



**HAL**  
open science

# Model-based dimensional NDE from few X-ray radiographs: Application to the evaluation of wall thickness in metallic turbine blades

Cédric Fragnaud, Clément Remacha, Julian Andrés Betancur Acevedo,  
Stéphane Roux

## ► To cite this version:

Cédric Fragnaud, Clément Remacha, Julian Andrés Betancur Acevedo, Stéphane Roux. Model-based dimensional NDE from few X-ray radiographs: Application to the evaluation of wall thickness in metallic turbine blades. Precision Engineering, 2024, 91, pp.536-545. 10.1016/j.precisioneng.2024.10.002 . hal-03777119v2

**HAL Id: hal-03777119**

**<https://hal.science/hal-03777119v2>**

Submitted on 7 Nov 2024

**HAL** is a multi-disciplinary open access archive for the deposit and dissemination of scientific research documents, whether they are published or not. The documents may come from teaching and research institutions in France or abroad, or from public or private research centers.

L'archive ouverte pluridisciplinaire **HAL**, est destinée au dépôt et à la diffusion de documents scientifiques de niveau recherche, publiés ou non, émanant des établissements d'enseignement et de recherche français ou étrangers, des laboratoires publics ou privés.

# Model-based dimensional NDE from few X-ray radiographs: Application to the evaluation of wall thickness in metallic turbine blades

Cédric FRAGNAUD<sup>1,2</sup>, Clément REMACHA<sup>2</sup>, Julián BETANCUR<sup>2</sup>, and Stéphane ROUX<sup>1</sup>

<sup>1</sup>Université Paris-Saclay, CentraleSupélec, ENS Paris-Saclay, CNRS,  
LMPS — Laboratoire de Mécanique Paris-Saclay, 91190, Gif-sur-Yvette, France

<sup>2</sup>Safran Tech, 78772 Magny les Hameaux, France

## Abstract

The extraction of 3D dimensional measurements based on a *limited* number of 2D X-ray radiographs of a part would offer a significant speed-up of quality control procedures in industry. However, there are challenges with respect to both measurements and uncertainties. This work addresses these challenges by creating an estimated numerical model of the imaged part on which dimensional measurements can be made. The numerical model is chosen as a parametric deformable model that encodes the expected shape variability of the parts resulting from the manufacturing process. The parameters and uncertainties of the numerical model of the imaged part are estimated by the registration of the computed projections of the model and the observed radiographs without the need of any segmentation. The registration requires the model, the initial parameters, and the observed radiographs. The proposed approach is applied to the inspection of turbine blades manufactured by investment casting, and in particular to the measurement of their wall thickness, which is a critical control. The deformable model consists in partitioning the inner ceramic core into multiple subparts, which may undergo a rigid body motion with respect to the master die. Wall thickness measurements are determined from the estimation of these rigid body motions. To assess the reliability of the proposed procedure, a repeatability study is performed. In addition, wall thickness measurements were compared to corresponding measurements from the surface of the metal boundary obtained by X-ray computed tomography. This surface was determined from a reconstructed tomogram using commercial software. Both analyses show that such measurements are reliable and efficient. Furthermore, residual differences between captured and computed projections reveal localized shape deviations from the CAD model, meaning that despite localized model errors, the approach is operable.

**Keywords** – Shape modeling, Shape parameter estimation, Deformation model, Metrology

## 1 Introduction

Non-destructive evaluation (NDE) is performed in the industry to control the quality of produced parts, ensuring that they meet their technical specifications. The increasing complexity of part geometry calls for the development of more advanced NDE methods. The necessity of NDE is even more stringent in sectors where safety is critical, such as aeronautics.

Turbine blades are key parts of aircraft engines. Their complex geometry is meticulously designed and optimized to improve the performance of the engine. Such an optimization addresses the overall aerodynamic efficiency and structural reliability [1], the isentropic efficiency [2], the adiabatic efficiency [3], or the stress and deformation [4] of the blades, through various approaches. In particular, internal air cooling features, such as rib turbulators, dimples, pin-fins or jet impingement [5], allow metal blades to operate at temperatures *higher* than their melting point, with combusted gas temperatures as high as 1500K [6], or turbine inlet temperatures found between 1700°C and 2000°C [7]. These extremely high temperatures are necessary to increase the power and fuel efficiency of aircraft engines. Turbine blades are fabricated following a high precision manufacturing process; nevertheless, geometrical indications — *i.e.* dimensional irregularities of the part that may result in a sub-optimal behavior of the engine — may

appear [8]. To ensure the structural integrity of the manufactured turbine blades, it is crucial to have high-precision measurements regarding their geometry for quality control.

Coordinate Measuring Machines (CMM) [9, 10] have been used to identify external dimensional imperfections. However, they are not suited to detect internal dimensional imperfections (such as cavities or just complex non-convex shapes). To this end, radiographic imaging methods, and in particular X-ray imaging, have been adopted. This non-destructive method enables the identification of voids, misalignment, perforations or material losses [11], the precise inspection of the internal cooling channels with a good contrast and resolution [12] and the wall thickness inspection with high accuracy [13]. The acquisition of a large number of X-ray radiographs, also called X-ray images, allows the 3D image (tomography or tomogram) of the part to be reconstructed through X-ray Computed Tomography (CT). X-ray CT involves taking multiple radiographs from different angles and combining them to create a detailed 3D representation of the part. By aligning the nominal model to the reconstructed volume, it is possible to compare the inspected part with its ideal design and extract measurements of deviation. Offering a complete 3D image of the inspected part, it appears as the gold standard for dimensional metrology. However, it suffers from some uncertainty, the main source of which being the thresholding of the gray scale image which may lead to a misidentification of material boundaries. Additionally, an inappropriate choice of the threshold causes a *systematic* error by either thickening or thinning the part. The proposed approach eliminates this uncertainty factor by not requiring any thresholding operations on tomograms. In addition, such an inspection requires a long acquisition and processing time. In contrast, inspection using X-ray radiography typically involves capturing a limited number of 2D images from specific views. In production lines, each part is observed from these limited views. These images are then inspected by specialist operators seeking an unusual gray level difference indicating an irregularity of the part. The measurement of 3D indications from 2D radiographs remains a complex problem for which automated methodology and procedures are highly desirable.

This paper presents an NDE method exploiting a limited number of acquired X-ray images. It relies on the simulation of the X-ray images from a numerical model of the part using an adequate and calibrated projective model [14, 15]. The CAD model is extended to a parametric deformable model so that the computed projections of the inspected part are registered onto the acquired X-ray images. This registration is performed by comparing the gray levels of the two series of X-ray images — acquired and computed — without requiring the determination of contours from 2D images or surfaces from 3D tomograms. 3D measurements and the associated uncertainty can be computed on the corrected model, which corresponds to the deformable model computed for the optimal transformation parameters.

In techniques such as Digital Image Correlation, it has been shown that displacements in the range of  $10^{-3}$ – $10^{-2}$  could be measured when the kinematics is simple (*e.g.* a mere translation), and analyzed over a large region of interest [16, 17]. A similar situation is faced here, where the “motion” is the one that relates the position of a surface in the model as compared to reality. Therefore, the proposed approach has the potential to significantly achieve a sub-voxel accuracy.

Section 2 is devoted to describing the developed method. More specifically, a discussion regarding the studied dimensional control, namely the wall thickness measurement, is provided in section 2.1. There, a discussion is proposed on the uncertainty of kinematics based on rigid body motion. The method to identify the optimal transformation parameters is then presented in section 2.2. A deformable model derived from the manufacturing process of turbine blades is proposed in section 2.3. The parameter identification method and the deformable model are the key features that permit the generation of a corrected numerical model. A repeatability study to assess the reliability of the proposed approach to measure wall thicknesses of a turbine blade is formalized in section 2.4. It consists of the wall thickness measurement of various samples of a turbine blade, each inspection being repeated multiple times. Section 3 reports and discusses the results of this study. They reveal that, even with the presence of model errors, the method is capable of generating a corrected model and measurements comparable to the ground truth (tomogram for which surface determination is performed automatically using the VGSTUDIO MAX® software), which implies comparable calculated wall thicknesses.

## 2 Methods

An NDE procedure to compute variations in the wall thickness of turbine blades based on a limited number of X-ray images has been developed. It requires a deformable model  $M$  of the inspected part

whose shape is controlled by a set of *transformation parameters*. A registration methodology is proposed to identify the transformation parameters of a reference model of the imaged part that best describes the difference between computed projections and observed radiographs.

The principle of the studied dimensional control is introduced before discussing the model parametrization and the method employed to identify the optimal transformation parameters.

## 2.1 Wall thickness metrology

Wall thickness corresponds to the distance between two surfaces, whether internal or external,  $\mathcal{S}_1$  and  $\mathcal{S}_2$ . This distance  $W_{12}$  is classically defined as

$$W_{12} = \min_{\substack{\mathbf{p}_1 \in \mathcal{S}_1 \\ \mathbf{p}_2 \in \mathcal{S}_2}} \|\mathbf{p}_1 - \mathbf{p}_2\|_2 \quad (1)$$

where  $\mathbf{p}_1$  and  $\mathbf{p}_2$  correspond to points on surfaces  $\mathcal{S}_1$  and  $\mathcal{S}_2$ , respectively. This definition is, however, not very convenient from an operational point of view since  $\mathbf{p}_1$  (resp.  $\mathbf{p}_2$ ) has to visit the entire surface  $\mathcal{S}_1$  (resp.  $\mathcal{S}_2$ ), and the minimum may not be unique. Hence, in practice, further restrictions can be enforced on  $\mathbf{p}_1$  or  $\mathbf{p}_2$ . In the following, this distance is computed using the ‘‘Ray method’’ implemented in VGSTUDIO MAX<sup>®</sup> (Volume Graphics GmbH, v 2.2) as the surfaces of the part are flat and the recommendation from the software provider has been followed. Namely, an initial point  $\mathbf{p}_1^0$  is chosen along surface  $\mathcal{S}_1$ , together with a solid angle of possible search. The closest point to  $\mathbf{p}_1^0$  along surface  $\mathcal{S}_2$  is found, and denoted  $\mathbf{p}_2^1$ . Then, the role of the two surfaces is interchanged, and the closest point to  $\mathbf{p}_2^1$  along surface  $\mathcal{S}_1$  is sought (with the same solid angle restrictions), and its minimum is denoted  $\mathbf{p}_1^2$ . This process is repeated until convergence, where a stationary solution  $(\mathbf{p}_1, \mathbf{p}_2)$  is found. To avoid the points getting out of a neighborhood of the initial point  $\mathbf{p}_1^0$ , it is necessary to consider escape conditions where the process does not converge. In case of success, the resulting distance is noted as  $W_{12}(\mathbf{p}_1^0)$ . This procedure is applied successively for all mesh nodes that lie on surface  $\mathcal{S}_1$  as a starting point, and finally  $W_{12} = \min_{\mathbf{p}_1^0} W_{12}(\mathbf{p}_1^0)$ .

Although not strictly identical to the above mathematical definition, eq. (1), this estimate is highly precise. However, secondary minima may exist, so the algorithm initialization (or its sampling) may miss the global minimum. This risk cannot be excluded in principle, although the region where the global minimum may be found suffers no ambiguity in practice. Ultimately, this evaluation has been retained after careful neighborhood choice.

In the following, a specific class of transformation applied to the surfaces defining the deformation model will be considered, namely rigid body motions. A brief discussion about their uncertainty is proposed before assessing the fluctuation of wall thickness measurement resulting from a rigid body motion.

### 2.1.1 Rigid body motion uncertainty

The screw theory mathematically describes a rigid body motion [18] and can be represented by a rotation  $\mathbf{R}$  and translation  $\mathbf{T}(\mathbf{q})$  at an arbitrary point  $\mathbf{q}$ . Although  $\mathbf{R}$  is intrinsic, the translation depends on the chosen reference point  $\mathbf{q}$ . More precisely, if another point  $\mathbf{q}'$  is chosen, then  $\mathbf{T}(\mathbf{q}') = \mathbf{T}(\mathbf{q}) + \mathbf{q}'\mathbf{q} \times \mathbf{R}$ .

An aspect that deserves specific comments is the uncertainty of the measured rigid body motion. From image registration, a displacement field can be calculated which can be described by its average  $\mathcal{M}_{\mathbf{q}} = (\mathbf{T}(\mathbf{q}), \mathbf{R})$  and its fluctuation,  $\delta\mathcal{M}_{\mathbf{q}} = (\delta\mathbf{T}(\mathbf{q}), \delta\mathbf{R})$ . This fluctuation is characterized by a null expectation value and a covariance matrix  $\mathbf{C}_{\mathbf{q}}$ , embedding the rigid body motion uncertainty, composed of three terms, each of which is a  $3 \times 3$  matrix:

$$\begin{aligned} \mathbf{C}_{\mathbf{q}}^{(1)} &\equiv \langle \delta\mathbf{T}(\mathbf{q}) \otimes \delta\mathbf{T}(\mathbf{q}) \rangle \\ \mathbf{C}_{\mathbf{q}}^{(2)} &\equiv \langle \delta\mathbf{T}(\mathbf{q}) \otimes \delta\mathbf{R} \rangle \\ \mathbf{C}_{\mathbf{q}}^{(3)} &\equiv \langle \delta\mathbf{R} \otimes \delta\mathbf{R} \rangle \end{aligned} \quad (2)$$

where  $\langle \cdot \rangle$  denotes the average of the quantities within the angle brackets, and  $\otimes$  is the tensor product. The covariance matrix of the rotation, *i.e.*  $\mathbf{C}_{\mathbf{q}}^{(3)}$ , is intrinsic. Considering it is a symmetric positive matrix, it can be diagonalized in the basis of eigenvectors  $\mathcal{B}$ . However, the full covariance matrix  $\mathbf{C}_{\mathbf{q}}$  is not intrinsic.

In particular, the non-diagonal terms of the cross-correlation  $\mathbf{C}_{\mathbf{q}}^{(2)}$  depend on the chosen reference point  $\mathbf{q}$ . It can be shown that there exists a unique point, denoted  $\mathbf{q}^*$ , such that the antisymmetric part of  $\mathbf{C}_{\mathbf{q}^*}^{(2)}$  is exactly zero. A privileged frame of reference is then  $\mathbf{q}^*$  as the origin while the axes orientations are given by  $\mathcal{B}$ .

### 2.1.2 Uncertainty of the distance between surfaces

Rigid body motions are applied to the surfaces  $\mathcal{S}_1$  and  $\mathcal{S}_2$ . Because the definition of the distance between surfaces, eq. (1), is not affected by a global rigid body motion affecting both surfaces, only the relative displacement of one surface with respect to the other matters. Thus only  $\mathcal{S}_2$  may be considered to be moving while  $\mathcal{S}_1$  remains static. The uncertainty of the measurement of  $W_{12}$  results from the uncertainty of the rigid body motion affecting  $\mathcal{S}_2$ . This question is addressed subsequently.

Let  $\mathbf{p}_1^*$  denote the point on surface  $\mathcal{S}_1$  where the minimum distance to  $\mathcal{S}_2$  is found, at point  $\mathbf{p}_2^*$ . The surfaces are supposed to be smooth in the neighborhood of  $\mathbf{p}_1^*$  and  $\mathbf{p}_2^*$  (no angular edge or corner) so that the surface around them can be described as parabolic. After applying the transformation  $\delta\mathcal{M}_{\mathbf{q}}$  to  $\mathcal{S}_2$ , the shortest distance between the surfaces changes. Assuming the rigid body motion  $\delta\mathcal{M}_{\mathbf{q}}$  is of small amplitude, a first order expansion of the change in distance  $\delta W_{12}$  is found to be a translation along the normal common to both surfaces  $\mathbf{n} = \mathbf{p}_1^*\mathbf{p}_2^*/|\mathbf{p}_1^*\mathbf{p}_2^*|$ .

This translation is however not intrinsic as it depends on the point at which the rigid body motion is expressed (section 2.1.1). There exists a unique point  $\mathbf{q}^*$  for which the antisymmetric part of the cross-correlation between  $\delta\mathbf{R}$  and  $\delta\mathbf{T}(\mathbf{q}^*)$  in the covariance matrix is null. Thus this point is chosen to compute the statistics of the correlation  $\mathbf{C}_{\mathbf{q}^*}$ , and the orientation of the frame is chosen to be given by the above introduced basis of eigenvectors  $\mathcal{B}$ . The variance of  $\delta W_{12}$  then reads

$$\langle \delta W_{12}^2 \rangle = \left( \mathbf{C}_{\mathbf{q}^*}^{(1)} + |\mathbf{q}^*\mathbf{p}_2^*|^2 \mathbf{C}^{(3)} \right) : (\mathbf{n} \otimes \mathbf{n}) + \mathbf{C}_{\mathbf{q}^*}^{(2)} : ((\mathbf{q}^*\mathbf{p}_2^*) \otimes \mathbf{n}) \quad (3)$$

where  $:$  denotes the double dot product.

These findings rely on the assumption that surfaces are smooth in the neighborhood of  $\mathbf{p}_1^*$  and  $\mathbf{p}_2^*$ . Additionally, the determination of  $\mathbf{p}_i^*$  after the transformation  $\delta\mathcal{M}_{\mathbf{q}}$  requires the curvature tensor  $(\boldsymbol{\kappa}_1 + \boldsymbol{\kappa}_2 + W_{12} \boldsymbol{\kappa}_1 \boldsymbol{\kappa}_2)$  to be inverted, where  $\boldsymbol{\kappa}_1$  and  $\boldsymbol{\kappa}_2$  denotes the curvature tensor of surfaces  $\mathcal{S}_1$  and  $\mathcal{S}_2$ , respectively. When the two surfaces approach a flat configuration, the inversion give rise to high values, so that the first order approximation assumption must be carefully assessed. The curvature tensor may even become negative, in which case the determination of  $\mathbf{p}_i^*$  may be unstable. One should note that, even if the position of the points  $\mathbf{p}_i^*$  becomes variable, the distance  $W_{12}$  itself may remain well behaved, but firm conclusions using the above development rest on the assumption that the change in  $\mathbf{p}_i^*$  remains small.

Therefore, wall thickness should be computed on smooth surfaces and for which the curvature tensor  $(\boldsymbol{\kappa}_1 + \boldsymbol{\kappa}_2 + W_{12} \boldsymbol{\kappa}_1 \boldsymbol{\kappa}_2)$  is well-conditioned (stable inversion) to obtain consistent and reliable measurements. In the following, wall thickness is measured at measurement points located in the airfoil of the blade, in accordance with these recommendations.

## 2.2 Identification of transformation parameters

Transformation parameters are identified by registering numerically simulated X-ray projections onto the corresponding set of radiographs that constitutes the observations. It is thus essential to consider a simulation tool capable of producing realistic X-ray images accounting for multiple phenomena such as beam hardening and/or scattering, and the appropriate projection geometry [15]. The  $N$  acquired radiographs of the inspected part are denoted  $P_{\mathbf{a}}^n(\mathbf{x})$ ,  $n \leq N$ , where  $\mathbf{x}$  represents the pixel position and  $n$  is the index of the view (different views implying different orientations of the part). Let  $\Pi^n$  be the projection operator for the view  $n$  acting on the model  $M$ . The acquired images correspond to the projections of a modified version of the model polluted by noise

$$P_{\mathbf{a}}^n(\mathbf{x}) \approx \Pi^n[M(\mathbf{d})](\mathbf{x}) + \eta^n(\mathbf{x}) \quad (4)$$

where  $\mathbf{d}$  is the  $K$ -component vector containing the transformation parameters  $d_k$ , and  $\eta^n(\mathbf{x})$  denotes the acquisition noise. Because of the detector and the cone-beam geometry of the source, acquisition noise is not homogeneous and is characterized by a variance that depends on pixel localization, noted as

$V^n(\mathbf{x})$ . Although a dependence on  $n$  is not generally expected, the averaging of the images performed during the acquisition of the radiographs is likely to depend on the projection angle to compensate for different attenuations related to the part orientation. Working on the assumption of a white Gaussian noise  $\eta^n(\mathbf{x})$ , the maximum of the (log-)likelihood associated to the probability of obtaining the difference  $P_a^n(\mathbf{x}) - \Pi^n[M(\mathbf{d})](\mathbf{x})$  corresponds to the minimum of its L<sub>2</sub>-norm. Hence, the following cost function is introduced

$$\Psi(\mathbf{d}) = \sum_n \left\| \frac{1}{\sqrt{V^n(\mathbf{x})}} (P_a^n(\mathbf{x}) - \Pi^n[M(\mathbf{d})](\mathbf{x})) \right\|_2^2 \quad (5)$$

Minimizing this function with respect to  $\mathbf{d}$  leads to the identification of the optimal transformation parameters. The weight term involving  $V^n(\mathbf{x})$  accounts for local uncertainties brought by the noise. The weighted L<sub>2</sub>-norm in eq (5) is justified as being optimal for the acquisition noise. This problem is solved iteratively using a gradient descent algorithm. At iteration  $t$ , the correction vector  $\delta\mathbf{d}$  corresponds to small perturbations, so that the above cost function is linearized about the solution  $\mathbf{d}^t = \mathbf{d}^{t-1} + \delta\mathbf{d}$

$$\Psi_{\text{lin}}(\delta\mathbf{d}) = \sum_n \left\| \frac{1}{\sqrt{V^n(\mathbf{x})}} (P_a^n(\mathbf{x}) - \Pi^n[M(\mathbf{d}^{t-1})](\mathbf{x}) - \Pi^n[\nabla_{\mathbf{d}}M(\mathbf{d}^{t-1})](\mathbf{x}) \cdot \delta\mathbf{d}) \right\|_2^2 \quad (6)$$

where  $\nabla_{\mathbf{d}}M$  denotes the derivative of  $M$  with respect to  $\mathbf{d}$ . The projection residuals and the sensitivity fields are defined respectively as

$$\rho^n(\mathbf{x}) = P_a^n(\mathbf{x}) - \Pi^n[M(\mathbf{d}^{t-1})](\mathbf{x}) \quad (7)$$

$$s_k^n(\mathbf{x}) = \Pi^n \left[ \frac{\partial M}{\partial d_k}(\mathbf{d}^{t-1}) \right](\mathbf{x}) \quad (8)$$

Applying (7) and (8) in (6), the linearized cost function is rewritten as

$$\Psi_{\text{lin}}(\delta\mathbf{d}) = \sum_n \left\| \frac{1}{\sqrt{V^n(\mathbf{x})}} \left( \rho^n(\mathbf{x}) - \sum_k s_k^n(\mathbf{x}) \cdot \delta d_k \right) \right\|_2^2 \quad (9)$$

The vector minimizing (6), noted  $\delta\mathbf{d}^*$ , is

$$\delta\mathbf{d}^* = \mathbf{H}^{-1} \mathbf{b} \quad (10)$$

where the matrix  $\mathbf{H} = (H_{ij})$ , the Hessian of  $\Psi_{\text{lin}}$ , and the vector  $\mathbf{b} = (b_k)$  are given by

$$H_{ij} = \sum_n \sum_{\mathbf{x}} \frac{1}{V^n(\mathbf{x})} s_i^n(\mathbf{x}) s_j^n(\mathbf{x}) \quad (11)$$

$$b_k = \sum_n \sum_{\mathbf{x}} \frac{1}{V^n(\mathbf{x})} s_k^n(\mathbf{x}) \rho^n(\mathbf{x}) \quad (12)$$

This approach converges towards the minimum of the cost function (5), leading to the identification of the sought vector of transformation parameters  $\mathbf{d}$ . The analysis of the uncertainties in the computed optimal parameters is an indicator of their reliability and is used to assess the quality of the registration. Assuming that the residuals  $\rho^n(\mathbf{x})$  at convergence mostly contains noise  $\eta^n(\mathbf{x})$ , these uncertainties are extracted from the registration procedure. The uncertainties associated with the estimates  $\delta d_i$  together with their correlations are given by the covariance matrix  $C_{ij} = \langle \delta d_i \delta d_j \rangle$

$$\langle \delta d_i \delta d_j \rangle = \sum_{k,l} H_{ik}^{-1} H_{lj}^{-1} \sum_{n,m} \sum_{\mathbf{x},\mathbf{y}} s_k^n(\mathbf{x}) s_l^m(\mathbf{y}) \left\langle \frac{\eta^n(\mathbf{x})}{V^n(\mathbf{x})} \frac{\eta^m(\mathbf{y})}{V^m(\mathbf{y})} \right\rangle \quad (13)$$

The noise is assumed to be Gaussian and white (spatially and temporally uncorrelated) such that

$$\langle \eta^n(\mathbf{x}) \eta^m(\mathbf{y}) \rangle = \delta_{nm} \delta_{\mathbf{x}\mathbf{y}} V^n(\mathbf{x}) \quad (14)$$

where  $\delta_{..}$  denotes the Kronecker symbol. Using the previous expression, eq. (13) reads

$$C_{ij} = \langle \delta d_i \delta d_j \rangle = H_{ij}^{-1} \implies \mathbf{C} = \mathbf{H}^{-1} \quad (15)$$

The associated correlation matrix  $\mathbf{R}$  is defined as

$$R_{ij} = \frac{C_{ij}}{\sqrt{C_{ii} C_{jj}}} \quad (16)$$

## 2.3 Deformable model of a turbine blade

To best capture the shape of the part, it is necessary to consider a deformable model  $M$  describing the expected shape variability. If the chosen deformable model provides a large flexibility, it will involve many degrees of freedom, at the risk of rendering the registration procedure ill-conditioned or even ill-posed. The deformable model thus needs to contain a reasonable number of parameters while describing the desired range of shapes. A deformable model derived from the *a priori* information on the manufacturing process is ideal to mitigate the lack of information due to the limited number of views.

The internal air cooling cavity of a turbine blade describing the internal structure is manufactured by an investment casting process. A ceramic core reproducing the shape of the desired cavity is positioned in the injection mold, known as *master die*. A slight misalignment of the core results in thinner or thicker walls in different regions of the blade compared to its ideal CAD model. Moreover, the core and master die may expand or shrink during the manufacturing process due to thermal constraints, which leads to geometrical deviations with the blade CAD model. Another potential source of thickness variation is a manufacturing defect in the core or in the master die themselves. However, they are considered negligible as compared to those induced by the core misalignment.

This manufacturing process may be exploited to generate the deformable model. The model  $M$  consists in the partition of the part into two main subparts: the master die and the core. The shape of the core is then extracted from the master die (see Figure 1). This model can be enriched depending on the structure or the manufacturing process of the core, for instance by further dividing the core into subparts. In this study, the core has been partitioned into 5 subparts, as illustrated in Figure 1 (middle). Each subpart indexed by  $k$  is associated with a transformation denoted  $\tau_k$  that maps the model of the corresponding subpart into the corrected one. To correctly interpret transformations, they need to be expressed in the same frame of reference, for instance, that of the ideal part CAD model. A corrected model is obtained by applying the transformations  $\tau_k$  to each subpart.

The kinematics of the subparts that define a simple yet representative deformable model is given by a rigid body motion of the independent subpart  $k$  parametrized by  $(\mathbf{t}_k, \boldsymbol{\alpha}_k)$ .  $\mathbf{t}_k$  denotes the translation vector of the  $k^{\text{th}}$  subpart, and  $\boldsymbol{\alpha}_k$  its rotation with respect to the center of the bounding box surrounding the initial master die (black point on Figure 1 (right)) which coincides with the origin  $\mathbf{O}$  of the coordinate system of reference. To account for thermal shrinkage/dilatation of the core, an additional scale factor  $s$  affecting all subparts of the core is introduced. This representation assumes that the geometry of each individual subpart perfectly matches its CAD model without deformation of its surface. This parametric deformable model of the turbine blade takes advantage of information about the manufacturing process, and is well suited for NDE. Moreover, the parametric representation of the corrected model allows for a direct interpretation of the origin of possible deviations from the conceived nominal model, and hence it provides insights about the manufacturing process itself and keys for improving it.

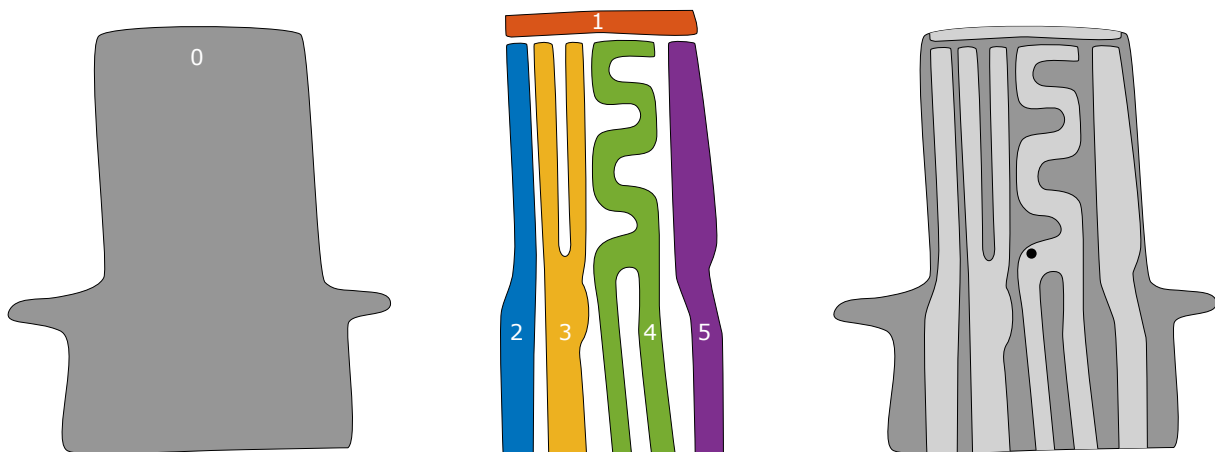


Figure 1: Illustration of the part divided into 6 subparts: the master die (left) and 5 subparts of the core (middle); and their association (right).

The estimation of the parameters  $s$  and  $(\mathbf{t}_k, \boldsymbol{\alpha}_k)$  is achieved following the procedure described in

Algorithm 1. The parameters are initialized from the ideal design of the core and of the master die. The convergence criterion is based on the norm of the residuals after each iteration.

---

**Algorithm 1:** Iterative registration procedure

---

**Input:** Meshes of each subpart, Initial estimates of parameters  $\mathcal{T}_c := (s, \mathbf{t}_1, \dots, \boldsymbol{\alpha}_5)$  and  $\mathcal{T}_0 := (\mathbf{t}_0, \boldsymbol{\alpha}_0)$

**Output:** Optimal values  $\mathcal{T}_c^* = (s^*, \mathbf{t}_1^*, \dots, \boldsymbol{\alpha}_5^*)$  and  $\mathcal{T}_0^* = (\mathbf{t}_0^*, \boldsymbol{\alpha}_0^*)$

- 1 Load meshes;
- 2 **do**
- 3     **for**  $k \leftarrow 0$  **to** 5 **do**
- 4         Apply the transformation  $\tau_k$  to the corresponding mesh of the  $k^{\text{th}}$  subpart;
- 5         Compute the sensitivity fields for  $\mathcal{T}_c$ ;
- 6         Compute the sensitivity fields for  $\mathcal{T}_0$ ;
- 7         Compute  $\delta\mathcal{T}_c^*$  using (10) from the sensitivity fields computed at lines 5;
- 8         Compute  $\delta\mathcal{T}_0^*$  using (10) from the sensitivity fields computed at line 6;
- 9         Update  $\mathcal{T}_c \leftarrow \mathcal{T}_c + \delta\mathcal{T}_c^*$  and  $\mathcal{T}_0 \leftarrow \mathcal{T}_0 + \delta\mathcal{T}_0^*$ ;
- 10 **while** *Convergence criterion reached*;

---

## 2.4 Repeatability study

A repeatability study was performed to assess the stability of the method and to evaluate the ability of the deformable model to cope with different parts. Indeed, the acquisition of X-ray images to control a part involves the manual positioning of the sample in the acquisition system which induces human variability. In practice, each control is then executed with a set of (slightly) different viewpoints. Because of their limited number, these viewpoints would contribute greatly to the determination of the transformations  $\tau_k$ . To eliminate the dependence on the sample positioning in the acquisition system, the transformation  $\tau_0^{-1}$  is to be applied to the computed corrected model. The idea behind this is to capture the *relative* motion of the core with respect to the master die, which fully determines the wall thickness. It also allows the computation of wall thicknesses in the same reference frame for all samples. This amounts to only applying the relative transformations  $\tau_k^0 := \tau_0^{-1}\tau_k$ ,  $k > 0$  to each subpart of the core. Although it theoretically solves the issue, it is essential for the reliability of the NDE procedure to validate this point.

During the repeatability study, X-ray images of six metallic turbine blades, selected so that they cover or exceed the tolerance interval for the wall thickness measurements, were acquired nine times each, after a complete tomography of each blade had been done to assess the actual wall thicknesses. The inspected turbine blades are referred to as samples in the following. The images were acquired at the Safran Advanced Turbine Airfoils (PFX) research center with an XT H 450 system developed by Nikon Metrology. The acquisition parameters are listed in Table 1. This tomograph has been qualified using strict industrial standards provided by a Metrologic Laboratory reference, namely the French National Laboratory of Metrology and Testing. During acquisition, the sample was manually positioned in the acquisition system and rotated by intervals of  $30^\circ$ , leading to a total of  $N = 12$  projections. The acquisition procedure was reproduced for all six samples and all nine repetitions.

For each batch of observed radiographs, the above described parametric deformable model was fitted using Algorithm 1 to generate a corrected model. Wall thickness was measured for 80 points in the airfoil, as mentioned in Section 2.1, using an automatic routine. Surfaces  $\mathcal{S}_1$  and  $\mathcal{S}_2$  introduced in eq. (1) correspond in practice to sub-surfaces around these measurement points. These sub-surfaces contain between 10 and 30 points each.

For each sample, nine sets of optimal transformation parameters were identified, one for each batch of images. A reasonable assumption of a Gaussian dispersion of the nine batches of transformation parameters allows the uncertainties on the measurements to be computed. This assumption was verified using Shapiro-Wilk normality test [19].

## 3 Results and discussion

The results of the repeatability study are discussed, and an illustration is provided as to how the information on residuals and transformation uncertainties could be exploited to assess the accuracy of the



Acceleration voltage	400 kV	Frames per projection	32
Tube current	500 $\mu$ A	Size of images	2000 $\times$ 2000 pixels
Pre-filtering	4 mm of copper	Voxel size	50.55 $\mu$ m
Exposure time	354 ms	Encoding	16-bit uint

Table 1: Parameters for X-ray image acquisition using the XT H 450 (Nikon Metrology).

model during inspection. Additionally, the concordance of the proposed method with X-ray tomography, the reference modality for wall thickness characterization, is evaluated.

### 3.1 Transformation across all samples

Figure 2 presents the average values of transformation parameters per sample in the repeatability study. The average was estimated over the nine repetitions. Each identified relative transformation  $\tau_k^0$  is a combination of a scaling by a factor  $s$ , a translation  $\mathbf{T}_k$ , and a rotation specified by Euler angles  $\boldsymbol{\theta}_k$ . It

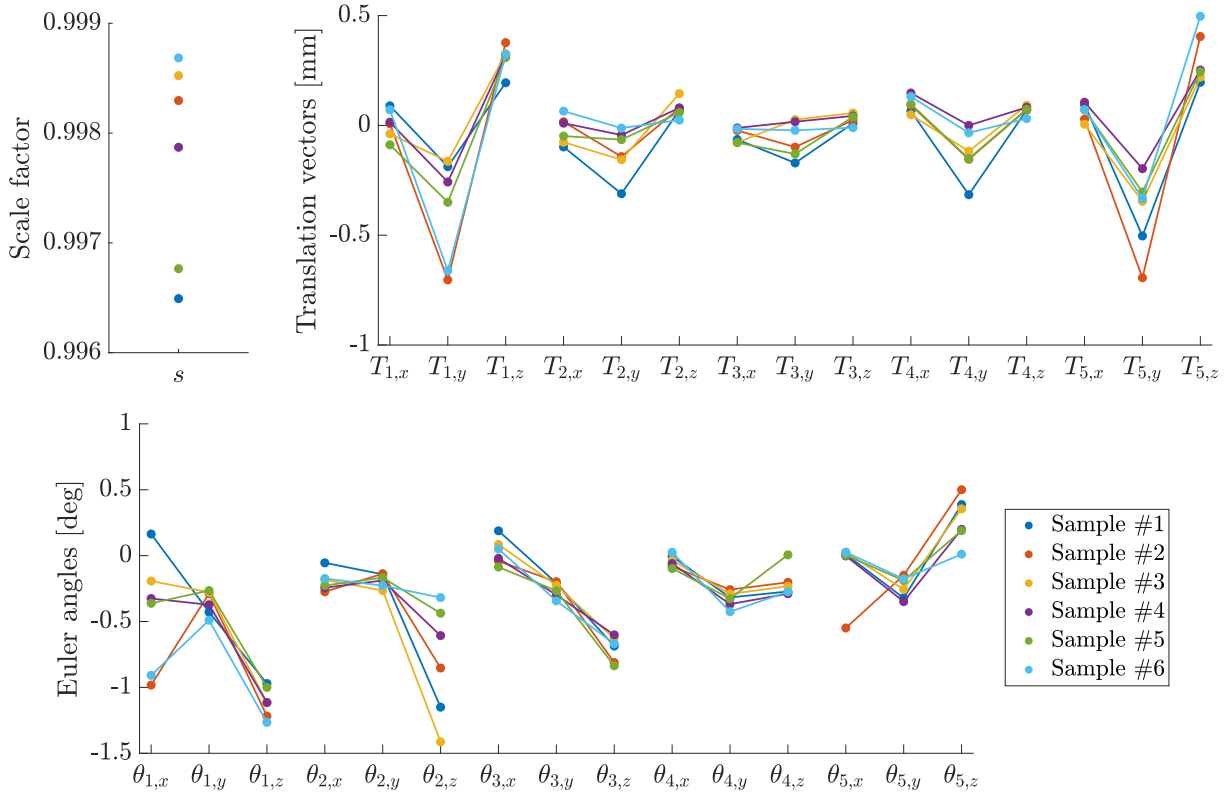


Figure 2: Average values of the transformation parameters for all samples: scale factor  $s$  (top left), components of the translation vectors  $\mathbf{T}_k$  (top right), Euler angles  $\boldsymbol{\theta}_k$  (bottom).

is observed that the transformation parameters display some variability between the different samples. This is due to the selection of the parts such that they would represent the production operating range. In this sense, Figure 2 describes the ability of the registration procedure to handle parts that have the same ideal design but whose actual geometry differs due to production variability. This highlights the relevance of the proposed approach to capture different model deformations.

In addition, considering that the transformation parameters are noticeable, it confirms the necessity of taking into account the rigid transformation of the core to perform accurate measurements of wall thicknesses. The large variability of the translation vectors  $\mathbf{T}_1$  and  $\mathbf{T}_5$  is due to the choice of the point about which rotations are computed (*cf.* subsection 2.1.1). For rigid body motions, translations are not intrinsic as they depend on the chosen point of rotation. As seen in Figure 1, subpart 1 (red) is far from

the center of rotation (black). The curved nature of the blade, not visible in Figure 1, leads to the same conclusion for subpart 5 (purple).

### 3.2 Transformation parameters for Sample #1

The variability of the identified transformation parameters for Sample #1 over the nine repetitions is presented in Figure 3. Values have been centered around their median  $m$  to better visualize their spread. The figure shows that the variability of the transformation parameters across repetitions are minute compared to the variability between samples: in the range of  $10^{-3}$  for the scale factor,  $35 \mu\text{m}$  for the translations parameters, and  $0.2^\circ$  for the Euler angles. Similar values were observed for all samples in the repeatability study. It should be emphasized that the variability in the translation parameter is smaller than the voxel size. This is made possible by the fact that the measurement is global and involves the entire Region of Interest, rather than individual points. As mentioned in the introduction, this property is well known in Digital Image Correlation, where uncertainties below  $10^{-2}$  pixel or less are routinely achieved.

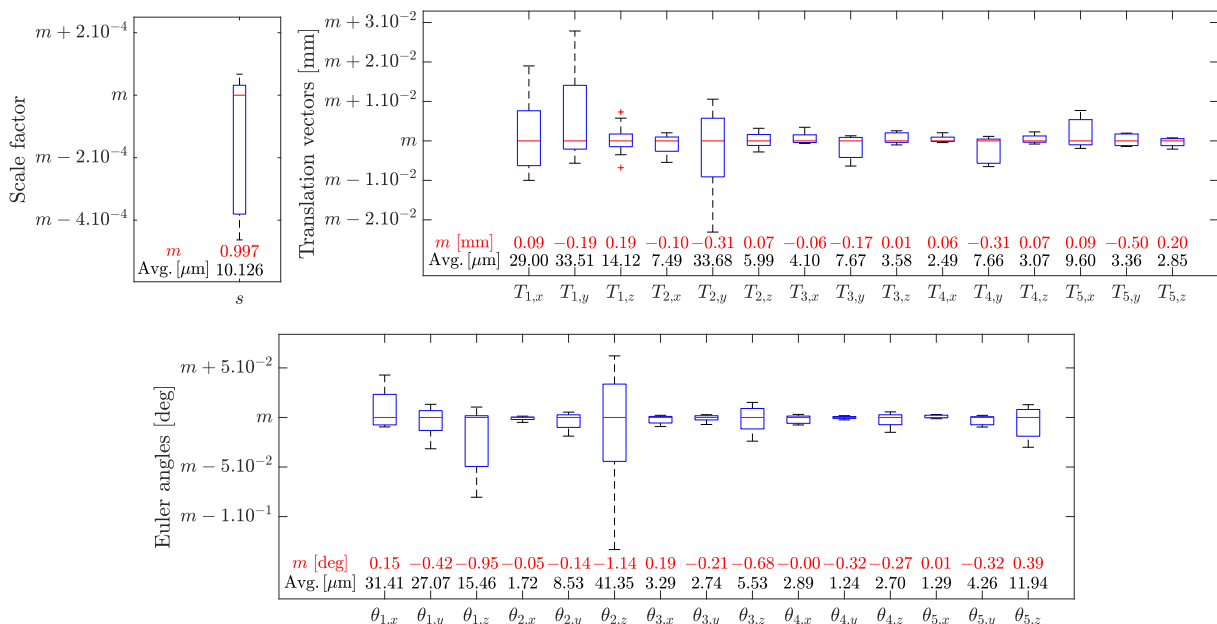


Figure 3: Boxplots showing the variability of the identified optimal transformation parameters over nine repetitions for sample number 1. Values have been centered around their median  $m$  to better visualize their spread. Below each box, the median value (red) and the average magnitude (in  $\mu\text{m}$ ) of the displacements associated with the observed variabilities (black) are presented.

The displacements associated with these observed variabilities need to be compared to the voxel size ( $50.55 \mu\text{m}$ , Table 1) for proper interpretation. Thus, for each parameter, two transformations are considered: one using the lowest identified value, and the other using the highest identified value, with the remaining parameters set to their respective medians. These transformations are applied to the initial model, and the magnitude of the displacement between the two transformed models is computed at each node of the mesh. For the rotation and translation parameters, this magnitude is averaged over the associated subpart; and for the scale factor, over the entire core. These values, expressed in  $\mu\text{m}$ , are reported below each box of Figure 3, in black (second line).

A high level of accuracy is observed for all parameters. Such accuracy is met thanks to the exploitation of the large number of pixels that make up the part in the radiographs acquired from different points of view, along with the prior knowledge of its shape. Combining these factors contributes to a more refined and precise estimate for transformation parameters that affect large-scale regions, reducing the variability to a sub-voxel level. The parameter  $\theta_{2,z}$ , for which the sub-voxel accuracy is barely met, exhibits the largest variability and, thus, uncertainty.  $\theta_{2,z}$  represents a rotation of the 2<sup>nd</sup> subpart, shown in blue in

Figure 1, around the  $Z$ -axis. This variability can be explained by the very elongated geometry of the subpart almost aligned with the  $Z$ -axis. As a consequence, any rotation about this axis induces a minute apparent motion in its projection. Because of this, the sensitivity field with respect to this parameter,  $\theta_{2,z}$ , is very small and contributes to bad conditioning of the Hessian matrix to be inverted. Ultimately, a Hessian eigenmode of low eigenvalue gives rise to a high variance in its measurement.

### 3.3 Projection residuals

Projection residuals are indicators of the effectiveness of the approach. Their analysis during production would enable to establish if the output model explains the acquired radiographs and, therefore, if it captures the shape of the part under inspection. Figure 4 displays projection residuals with the initial (top) and optimal (bottom) transformation parameters computed for one repetition on sample #1. The figure focuses on four areas of interest chosen for being representative of the entire field. Residual values are expressed as a percentage of the dynamic range of the observed projections. The higher level of residuals in the root of the turbine blade, panel (a), is explained by the fact that some phenomena, particularly visible for high thicknesses, were misestimated (*e.g.* Beam Hardening) or not included in the projection operator  $\Pi^n$  (*e.g.* diffraction). It should, however, be noted that this imperfection in the projection operator is small as it represents, at most, in the thickest area, a 5.6% deviation from the gray levels of the observed projections. In the top row, the observed residuals are mainly due to the deviation of the core from its ideal design, as shown, for instance, in panel (c)-top where a structure with positive residuals on the left and negative on the right is visible. Similar structures are apparent on the other panels. These deviations are accounted for by the introduced degrees of freedom. Thus, in the bottom row, the above-described structure visible on panel (c) is highly reduced, as well as for the other panels. The procedure leads to the estimates of the best transformation parameters considering the proposed parametrization and is deemed validated for all computed residuals.

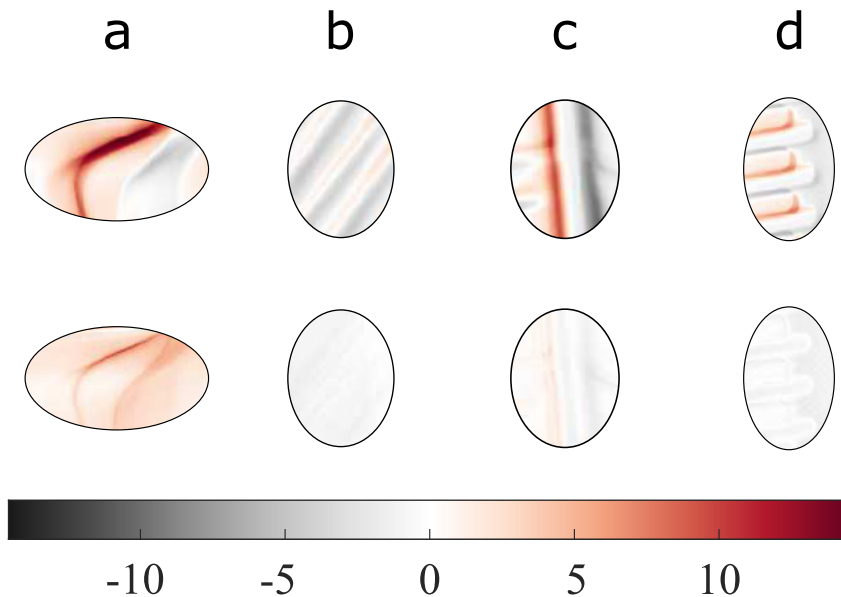


Figure 4: Color-coded difference between acquired and simulated projections, before (top) and after (bottom) identification of the transformation parameters. The different panels show (a) a curved region in the root of the turbine blade, (b) an internal structure, known as a rib structure, in the airfoil, (c) the wall of an internal cavity, (d) slots on the trailing edge of the blade. Values are expressed as a percentage of the dynamic range of the observed projections.

### 3.4 Covariance and correlation matrices

Using equation (15), the covariance matrices  $\mathbf{C}$  are computed. An example of such a matrix is displayed in Figure 5, together with the associated correlation matrix  $\mathbf{R}$ .

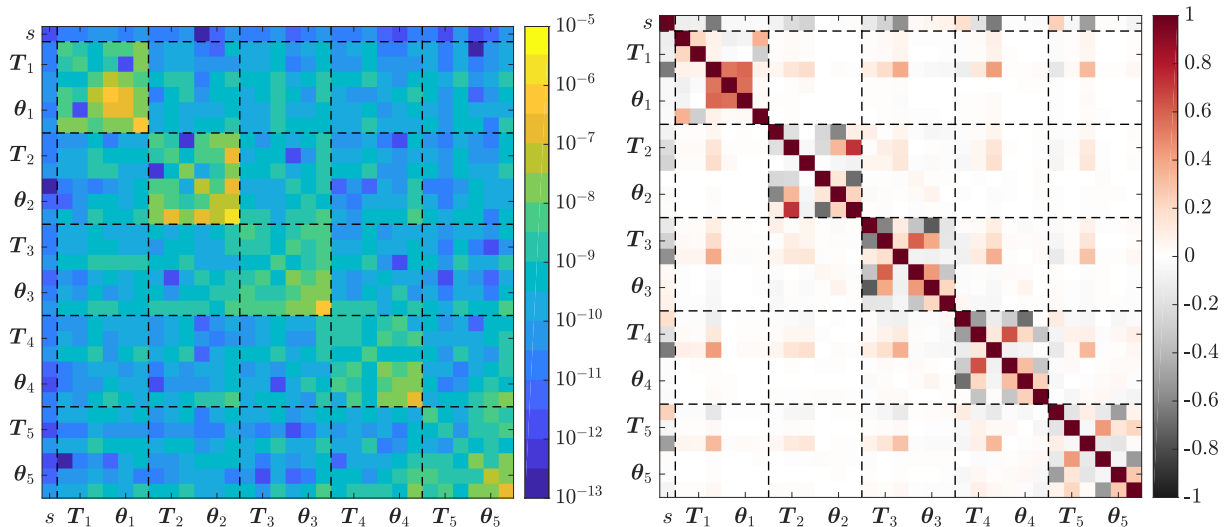


Figure 5: Element-wise absolute value of the covariance matrix  $\mathbf{C}$  (left, logarithmic scale) and correlation matrix  $\mathbf{R}$  (right) computed at convergence. Black dotted lines are plotted to better visualize the different subparts.

By definition, the diagonal terms of the correlation matrix  $\mathbf{R}$  are equal to 1. Non-diagonal terms, which range from  $-1$  to  $1$ , represent the degree of correlation (or anti-correlation when negative) between a pair of parameters. As expected, parameters associated with distinct subparts are weakly correlated (less than  $0.5$ ). The scale factor  $s$  is mostly (negatively) correlated to the translation parameter along the main orientation of the subpart, as a result of its slenderness.

The displacement  $\mathbf{u}(\mathbf{x})$  of any point  $\mathbf{x}$  at the surface of a subpart can be written as a linear combination of the transformation parameters,  $\mathbf{u}(\mathbf{x}) = \mathbf{a}(\mathbf{x}) \cdot \mathbf{d}$ . The uncertainty on the estimation of this particular displacement is readily accessible from the covariance matrix: the variance on  $\mathbf{u}$  is  $\sigma^2(\mathbf{x}) = \mathbf{a}(\mathbf{x})^\top \mathbf{C} \mathbf{a}(\mathbf{x})$ . Similarly, the expression of the covariance between the displacement of two points can be very easily computed from  $\mathbf{C}$ .

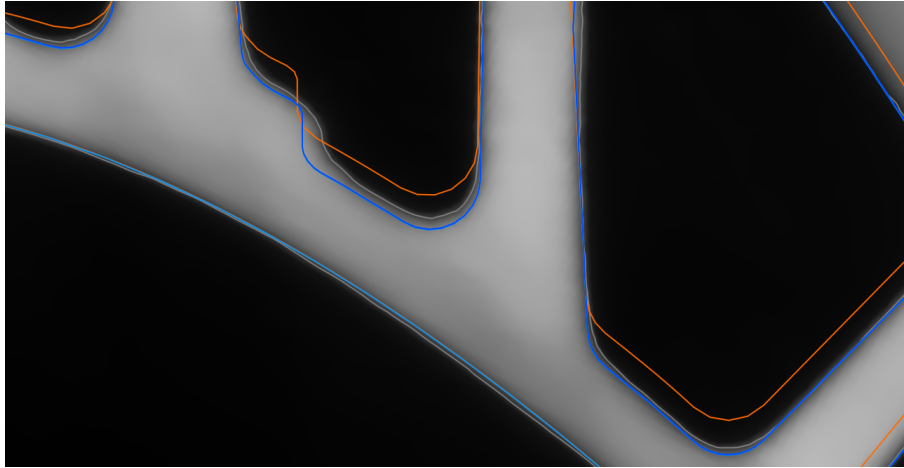
### 3.5 Shape comparison with ground truth (tomogram)

The transformed CAD models are compared to the ground truth given by a tomographic volume reconstructed from a set of 3000 radiographs. Figure 6 displays the tomogram (gray) with the initial CAD model (orange) and corrected ones (different shades of blue are used for all nine estimates for sample #1). It can be seen that the blue surfaces line up more tightly with the boundaries of the tomogram than those of the initial CAD model. Discrepancies are observed for the cavity in view (a) or the rib in view (c), which appear shifted. As displayed in Figure 6, these areas are characterized by a high curvature of the surfaces. Moreover, the surfaces of these cavities are inclined at a low angle with respect to the section planes, further amplifying the discrepancy in those section views. The offset between the surfaces can be measured to be about one or two voxels. Let us emphasize the remarkable agreement between the corrected model and the tomogram (when the curvature is low), despite the drastic reduction in the number of radiographs by a factor of almost 300.

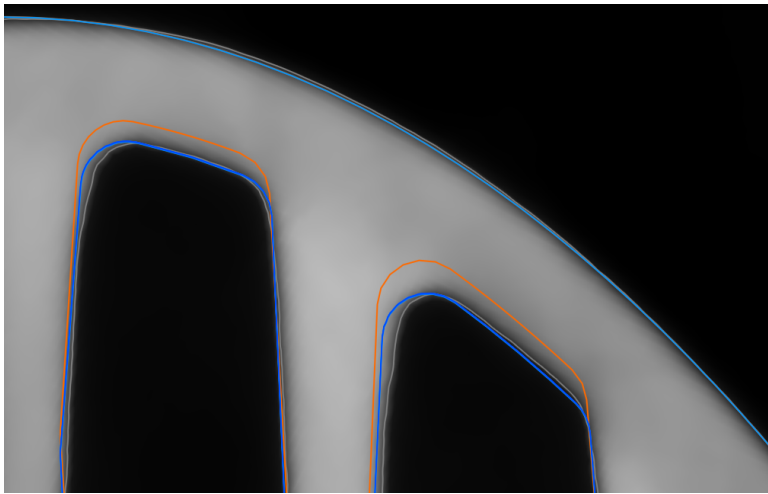
Some remaining deviations are observed. In view (c), the CAD design displays sharp corners, whereas the ones in the manufactured part are smoother. This discrepancy can be explained by the effect of the sintering of the mold or the surface tension between the metal and the core during metal casting. As these phenomena are not described in the deformable model, such deviations cannot be resolved.

Thus, even with (hopefully localized) model errors, the proposed deformable model explains most of the differences, which renders the correction efficient and operable. In addition, the observed differences between the part and its CAD model in highly curved regions point towards considering other deviations from the original CAD model, namely non-rigid shape deformations. These deviations may be accounted for by resorting to a more flexible deformable model, for instance, an additional correction model acting at

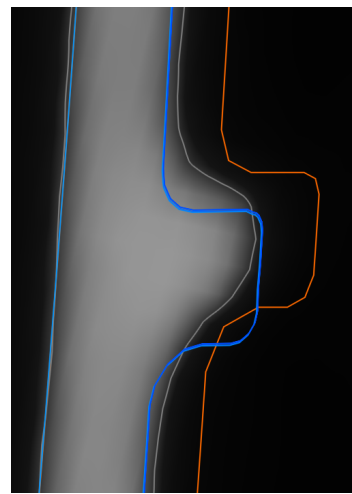
a more local scale. An alternative would be to use a more representative core mesh obtained from actual manufactured cores. Such a procedure would allow us to distinguish more clearly between systematic shape deviation due to the manufacturing process and intrinsic variability. In the case where the geometry of the subparts are systematically measured in the control chain, *e.g.* by Non-Contact CMM, this approach would allow one to increase the available *a priori* information without increasing the time allocated for the control. Introducing a local weighting of the surfaces based on their curvature and incorporating it into an additional weight term in eq. (5) can also be considered to further reduce the impact of these model errors.



(a)



(b)



(c)

Figure 6: Superimposition of the ideal (orange) and transformed (shades of blue) designs of the core over the tomogram (gray).

### 3.6 Concordance of wall thickness measurements by model-based NDE and by tomogram

Wall thicknesses have been measured in the airfoil of the nine corrected models of sample #1 and of the tomogram, at 90 particular locations to sample the statistical dispersion. As visually suggested by Figure 6, measurements of the transformed models are similar, such that the average values of the measurements are shown for further data acquisition and processing. Figure 7 (left) shows a Bland-Altman plot [20] to illustrate the disagreement between the two measurement methods. The bias of 26.6  $\mu\text{m}$  indicates the average difference between the two measurement methods. This discrepancy represents slightly more

than *half a voxel*, showing the high accuracy of the proposed approach. The limits of agreement, which indicate the precision of the measuring system, are to be compared to the tolerance values defined in the part specification. In the case of aeronautical parts for which dimensional compliances are very stringent, this large interval of  $\approx 196 \mu\text{m}$  does not meet the technical requirements. For the sake of comparison, the same measurements have been performed on the untransformed model (see Figure 7 right). Using the proposed approach, the bias is increased by a slight amount of  $15 \mu\text{m}$ , while the limits of agreement are significantly reduced by  $185 \mu\text{m}$ . It should, however, be noted that a less constrained parametrization of the shape would be likely to yield a transformed model closer to reality and, thus, more accurate measurements.

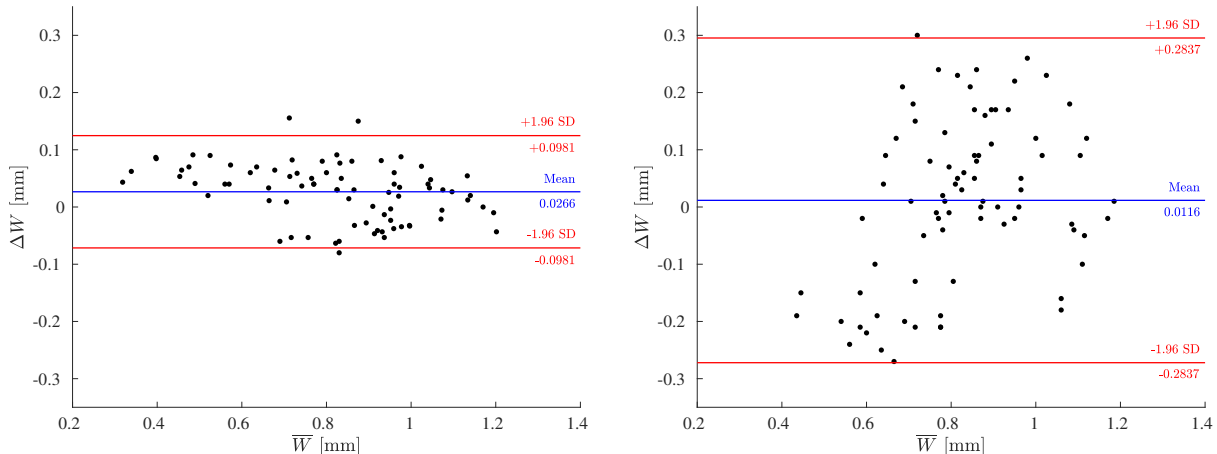


Figure 7: Bland-Altman plot of wall thickness measurements by the proposed model and by X-ray CT tomography. The plot displays the difference  $\Delta W$  as a function of the mean value  $\bar{W}$  of measurements using the corrected (left) and initial (right) models. The mean of the differences (blue line) indicates the bias between the values obtained from the two measurement methods. The limits of agreement (red lines) delineate the interval where 95% of the differences are expected to lie.

The computation of measurement uncertainties based on the covariance matrix  $\mathbf{C}$  produced estimates of the order of a few hundred nanometers, which is significantly lower than the uncertainty values obtained by repeating the same control several times. The formula (13) used for the computation of  $\mathbf{C}$  relies on the assumption that the residual  $\rho^n$  mostly contains noise  $\eta^n$ . For this assumption to be verified, it is necessary to have a transformed model that exactly matches the imaged part and a perfect projection operator. From the previous results, it appears that these two conditions are not met as the shape of each surface differs between the CAD model and each sample because of the fabrication process. Figure 6 displays differences in geometry between the estimated model and the ground truth, mainly because the non-rigid deformation of the core is not included in the deformable model.

### 3.7 Limitations

The findings of this study do have some limitations. A limitation of the approach is that the proposed deformable model is presumably too simple to account for all sources of shape mismatch. Ideally, a flexible model would be required. However, an important feature is the parametrization of the considered deformation modes. The ones considered in this work (independent rigid body motions) benefit from a parametrization that is neither too rich (large uncertainty) nor too poor (realism of shape deviations). It is this trade-off that motivated the decision to define the modes as independent rigid body motions. This trade-off leaves a margin of error which leads to residual shape deviations between the transformed model and the tomogram and, thus, unreliable measurements. To improve the set of transformations, one may envision a more flexible deformable model, adding a local correction model or replacing CAD models of the surfaces with measured ones. Furthermore, projection residuals (above denoted  $\rho^n$ ) are indicators of the registration quality and, thus, of the reliability of the computed measurements. They may also be used to identify the most appropriate locations for the measurement points.

It is worth noticing that the images were acquired in a single X-ray cabin (XT H 450), which may constitute a bias in the analysis. Likewise, the procedure was tested on parts of a single type, *i.e.* a single reference of a turbine blade, even if multiple samples were imaged to account for shape variability. It is, however, expected that similar results would be observed for a different acquisition system or reference of a turbine blade with a comparable manufacturing process, as no other assumptions other than the manufacturing process have been made. However, accounting for *e.g.* the panel detector used in the X-ray cabin may enrich the projection operator. From an industrial point of view, endorsing the procedure would require that the same study be performed with multiple parts to ensure that a change in the blade geometry would not lead to inconsistent results. Nevertheless, nothing currently suggests that additional issues are to be encountered.

The time needed to estimate parameters is about 5-6 hours. This figure is only indicative since the code was not optimized, as the feasibility and potential of the method was the main objective of this study. In particular, costly voxelization (estimated to take about 3 hours alone) and voxel-based projection were used. In the latest release of the Astra toolbox [21], the CAD model (or its mesh) can directly be used, resulting presumably in a significant speed-up, but this option was not tested. Estimating uncertainties, performed only at the last iteration, is very fast.

## 4 Conclusion

In this work, an approach to assess 3D dimensional measurements of complex shape parts from a limited number of 2D X-ray images has been presented. It consists of fitting a parametric model of the imaged part to generate a corrected numerical model. The dimensions to be controlled are measured directly on this corrected model. The selected application case is the control of wall thicknesses of a hollow turbine blade, a part with complex internal geometry. Describing the control principle allowed the definition of guidelines to perform reliable measurements. The optimal transformation parameters of the model are identified by iteratively matching the projections simulated from the transformed model to the observed projections. The parametric model has been developed in line with the manufacturing process. It relies on the partition of the part into multiple subparts: one representing the external surface, five representing the various element of the inner ceramic core describing the internal geometry. The kinematics of each subpart is a rigid-body motion, plus a scale factor to account for thermal constraints experienced by the ceramic core during metal casting. This sparse model mimics what occurs during manufacturing and thus provides a fair description of the expected shape variabilities. In addition, the observed transformations can be further exploited to improve the manufacturing process and reduce the range of shape deviations.

The reliability of the approach was verified *via* a repeatability study where only a slight discrepancy in the identified parameters, and thus in the associated corrected models, was observed. Furthermore, the agreement between measurements computed from the transformed models and reference values computed from a tomogram demonstrated the approach performance. Discrepancies are mostly explained by the non-rigid shape deformations not considered in the simple deformable model proposed here. These discrepancies, although small, do not comply with the very demanding requirements for NDE of turbine blades. Suggestions to mitigate the discrepancy are proposed and include the use of measured surfaces, or the introduction of a more flexible deformable model.

It is worth emphasizing that the proposed methodology has been designed to minimize the acquisition noise error, as expressed in eq. (5). This error is currently much lower than other elements of uncertainty and as a consequence, the method leads to an over-quality. One can consider faster, therefore noisier, acquisitions while still remaining below the uncertainties due to other factors. Let us also stress that the entire procedure is automated, with no specific input from the operator (and hence no particular skill or experience is required), after criteria for shape tolerance have been set.

GUM methodology [22] offers a rigorous framework for taking into account a multiplicity of operations, each affecting the final (expanded) uncertainty of a measurement. The proposed thickness measurement can be viewed mostly as an elementary operation, for which a careful assessment of the uncertainty has been performed, through what can be regarded as the first steps of the GUM method (identifying detector noise as the main source of uncertainty, modeling the measurement, and computing the resulting uncertainty due to noise on the result). This procedure could be embedded into a wider framework adding other sources of uncertainty, and combining them with those studied in the manuscript.

## Acknowledgement

This work was supported by the French “Association Nationale de la Recherche et de la Technologie” (CIFRE n° 2019/0793). The first and second authors would like to thank Mr. Omer Unlu and Mr. Pierre-Luc Patard for their implication in the experimental phase. The authors would like to thank Ms. Tonya Rose from the Digital Sciences and Technologies Department at Safran Tech for her insightful suggestions on the manuscript.

## References

- [1] Clemens Buske, Alexander Krumme, Thomas Schmidt, Christian Dresbach, Sascha Zur, and Rüdiger Tiefers. Distributed Multidisciplinary Optimization of a Turbine Blade Regarding Performance, Reliability and Castability. In *Turbo Expo: Power for Land, Sea, and Air*, volume 49712. American Society of Mechanical Engineers Digital Collection, 2016.
- [2] Mathias Luers, Max Sagebaum, Sebastian Mann, Jan Backhaus, David Grossmann, and Nicolas R. Gauger. Adjoint-based Volumetric Shape Optimization of Turbine Blades. In *2018 Multidisciplinary Analysis and Optimization Conference*. American Institute of Aeronautics and Astronautics, 2018.
- [3] Jiaqi Luo and Yao Zheng. Aerodynamic Shape Optimization of a Turbine Blade Considering Geometric Uncertainty Using an Adjoint Method. In *Turbo Expo: Power for Land, Sea, and Air*, volume 58578. American Society of Mechanical Engineers Digital Collection, 2019.
- [4] Chun-Yi Zhang, Ze Wang, Cheng-Wei Fei, Zhe-Shan Yuan, Jing-Shan Wei, and Wen-Zhong Tang. Fuzzy Multi-SVR Learning Model for Reliability-Based Design Optimization of Turbine Blades. *Materials*, 12(15):2341, 2019.
- [5] Farah Nazifa Nourin and Ryoichi S. Amano. Review of gas turbine internal cooling improvement technology. *Journal of Energy Resources Technology*, 143(8):080801, 2021.
- [6] S. Dhivya and A. Karthikeyan. Design and Analysis of Gas Turbine Blade with Cooling. *EAI Endorsed Transactions on Energy Web*, 5(20), 2018.
- [7] Mohammed Aljibory, Farhan Lafta, and Hasan Qahtan. Review Of Heat Transfer Enhancement In Air-Cooled Turbine Blades. *International Journal of Scientific & Technology Research*, 9:3123–3130, 2020.
- [8] Jonas Aust and Dirk Pons. Taxonomy of Gas Turbine Blade Defects. *Aerospace*, 6(5):58, 2019. Publisher: Multidisciplinary Digital Publishing Institute.
- [9] Robert J. Hocken and Paulo H. Pereira. *Coordinate measuring machines and systems*, volume 6. CRC press Boca Raton, FL, 2012.
- [10] Grzegorz Budzik. Geometrical accuracy of aircraft engine turbine blades. *Oficyna Wydawnicza Politechniki Rzeszowskiej, Rzeszów*, 2013.
- [11] Radosław Przysowa, Marek Chalimoniuk, Danuta Grzelka-Gajek, Ruslan Shakalo, and Artem Karpenko. CT Inspection of Cooled Turbine Blades. *Journal of KONBiN*, 50(3):307–331, 2020.
- [12] Józef Błachnio, Marek Chalimoniuk, Artur Kułaszka, Henryk Borowczyk, and Dariusz Zasada. Exemplification of detecting gas turbine blade structure defects using the X-ray computed tomography method. *Aerospace*, 8(4):119, 2021.
- [13] Scott Hastie, Anthony Chan, Kevin Wiens, Doug Nagy, Robert Tollett, and Paul Lowden. Computed Tomography Wall Thickness Inspection to Support Gas Turbine Blade Life Extension. In *Turbo Expo: Power for Land, Sea, and Air*. American Society of Mechanical Engineers Digital Collection, 2021.
- [14] Wim Van Aarle, Willem Jan Palenstijn, Jeroen Cant, Eline Janssens, Folkert Bleichrodt, Andrei Dabravolski, Jan De Beenhouwer, Kees Joost Batenburg, and Jan Sijbers. Fast and flexible X-ray tomography using the ASTRA toolbox. *Optics express*, 24(22):25129–25147, 2016. Publisher: Optical Society of America.



- [15] Cédric Fragnaud, Clément Remacha, Julián Betancur, and Stéphane Roux. CAD-based X-ray CT calibration and error compensation. *Measurement Science and Technology*, 33(6):065024, 2022.
- [16] François Hild and Stéphane Roux. Comparison of local and global approaches to digital image correlation. *Experimental mechanics*, 52(9):1503–1519, 2012.
- [17] Stéphane Roux and François Hild. Comprehensive full-field measurements via Digital Image Correlation. *Comprehensive Mechanics of Materials*, 2024.
- [18] Fedor Menas'evich Dimentberg. *The Screw Calculus and Its Applications in Mechanics*. Air Force Systems Command. FTD, Foreign Technology Division. Foreign Technology Division, WP-AFB, 1968.
- [19] Samuel Sanford Shapiro and Martin Bradbury Wilk. An analysis of variance test for normality (complete samples). *Biometrika*, 52(3/4):591–611, 1965.
- [20] John Martin Bland and Douglas Graham Altman. Statistical methods for assessing agreement between two methods of clinical measurement. *The lancet*, 327(8476):307–310, 1986. Publisher: Elsevier.
- [21] Pavel Paramonov, Nicholas Francken, Jens Renders, Domenico Iuso, Tim Elberfeld, Jan De Beenhouwer, and Jan Sijbers. CAD-ASTRA: a versatile and efficient mesh projector for X-ray tomography with the ASTRA-toolbox. *Optics Express*, 32(3):3425–3439, 2024.
- [22] OIML. *Guide to the Expression of Uncertainty in Measurement*. Joint Committee for Guides in Metrology, 2023.